Testing for Welding, Joining or Additive Manufacturing Applications

İstemihan Gökdağ* and Erdem Acar

Effects of process parameters on strengthening mechanisms of additively manufactured AlSi10Mg

https://doi.org/10.1515/mt-2022-0449

Abstract: In industries like automotive and aerospace, the demand for structures with a high strength-weight ratio is increasing. Additive manufacturing (AM) studies and applications of AlSi10Mg material have increased due to the improvement of mechanical properties when the production is performed at high cooling rates in the laser-powder bed fusion (L-PBF) method. The study aims to investigate the effect of the AM process parameters on the microstructure features, and determine the mathematical relationship between yield strength and process parameters to obtain better mechanical properties. In this study, AlSi10Mg specimens are manufactured using L-PBF method with different process parameters. Microstructure images of the manufactured specimens are obtained by scanning electron microscopy. Melt pool width, eutectic cell size and diameter of Si precipitates are measured using the microstructure images. Parametric equations are generated between the process parameters and microstructural features including eutectic cell size and Si precipitate diameter. Thus, relationships between strengthening mechanisms and process parameters are established by integrating the generated equations into the related strengthening mechanisms. Consequently, the yield strength model of AlSi10Mg material is developed as a function of the process parameters of L-PBF method. It is found that the developed model estimates close results to the nano-indentation results.

Keywords: additive manufacturing; aluminum alloys; laser-powder bed fusion; microstructure; strengthening mechanisms.

***Corresponding author: İstemihan Gökdağ**, Additive Manufacturing Division, Turkish Aerospace Industries Inc., Ankara, Türkiye; and Department of Mechanical Engineering, TOBB University of Economics and Technology, Sogutozu Cad. No:43, Cankaya, Ankara, 06560, Türkiye, E-mail: istemihan.gokdag@tai.com.tr. https://orcid.org/0000-0002-1481-5572

Erdem Acar, Department of Mechanical Engineering, TOBB University of Economics and Technology, Sogutozu Cad. No:43, Cankaya, Ankara, 06560, Türkiye. https://orcid.org/0000-0002-3661-5563

1 Introduction

Additive manufacturing (AM) is a manufacturing method that creates 3D objects by adding material layer-by-layer [1]. Metal AM methods have been widely used in structural applications of automotive and aerospace industries due to their ability to produce lightweight, optimized and complex designs [2–4]. Al alloys are frequently used in industries to produce parts with a high strength-weight ratio [5–7]. In the laser powder bed fusion (L-PBF) method, manufacturing is processed at high cooling rates (10^3–10^8 K s^{-1}) resulting fine microstructures. Thus, the structures with higher mechanical properties can be produced by using L-PBF [8–10].

Previous studies have investigated the change of the AlSi10Mg microstructures manufactured with different L-PBF process parameters and cooling rates. Delahaye et al. [9] revealed the effects of thermal gradient on melt pool and heat-affected zone as well as the variations in the size and distribution of Si precipitates in different zones of the microstructure. Hyer et al. [11] studied the microstructural changes of AlSi10Mg fabricated with different process parameters. Their research showed that size and shape of melt pool, cell size as well as the relative density of the specimens varied depending on the process parameters. Narra et al. [12] investigated the relationship between melt pool, cell spacing and cooling rate with an experimental study to control additive manufacturing processes. Maamon et al. [13] presented hardness variation of as-built AlSi10Mg manufactured with L-PBF according to laser power, scan speed, hatch spacing and energy density, respectively. Wu et al. [14] investigated the effects of process parameters on the melting modes and the relationship between microstructure and mechanical properties using the AlSi10Mg samples manufactured with different energy densities. The effects of heat treatment processes have been investigated on the microstructure of AlSi10Mg to improve mechanical properties [15, 16]. Finally, process parameter studies have been performed to optimize the mechanical properties and to obtain sound microstructure [17, 18].

It is necessary to investigate the strengthening mechanisms of AlSi10Mg to deeply understand the changes in mechanical properties according to the cooling rate and process

parameters. During the deformation of AlSi10Mg material, dislocations accumulate at the eutectic cell boundaries and around the Si precipitates and resist deformation [19]. Strengthening mechanisms of AlSi10Mg processed by L-PBF with adding nano-TiB2 are determined as Hall–Petch (H-P), Orowan and load-bearing mechanisms [20]. The Orowan strengthening mechanism is identified as the most effective mechanism to improve the strength of the AlSi10Mg [21]. Hadadzaded et al. [22, 23] reported that similar results to the tensile test results can be obtained by using H-P, Orowan as well as dislocation-hardening mechanisms for AlSi10Mg processed by L-PBF. Finally, it is reported that microstructural features like grain and cell structures of AlSi10Mg are not affected by thermal cycles during the solidification process [24].

The current literature lacks a detailed description of the effects of the process parameters of AM on strengthening mechanisms of AlSi10Mg processed by L-PBF. The study aims to fill this gap by establishing a mathematical relationship between process parameters and microstructural as well as mechanical properties including a detailed investigation of microstructural properties. This paper is organized as follows: the methodologies of L-PBF manufacturing, measuring of melt pool, eutectic cell size, Si precipitate and nano-indentation (NI) are described in Section 2. Variations of microstructural features of AlSi10Mg including cell size and Si precipitates according to laser power, scanning speed and energy density are also investigated in Section 2. According to the experimental results, parametric equations are generated and the equations are integrated into H-P and Orowan strengthening mechanisms in Section 3. A comparison of the generated yield strength model and NI test results is also presented in Section 3. Additionally, the relation between melt pool and process parameters is investigated using the experimental results in Section 3. Finally, the conclusions drawn from this study are presented in Section 4.

2 Methodology

2.1 L-PBF process

The specimens are manufactured using Concept Laser M2 Cusing machine with 400 W ytterbium (Yb) fiber laser under argon atmosphere in this study. Scanning speed and laser power are determined as design variables to examine their effects. For each parameter, three levels are considered (see Table 1). Full factorial design (FFD) of experiments is used, and specimens with the dimensions of $10 \times 10 \times 10$ mm are manufactured. Powder provided by Concept Laser Company is used in manufacturing. The other process parameters are kept constant during manufacturing (see Table 2).

Table 1: Process parameters (variables) and levels.

Variable	Laser power (W)	Scanning speed (mm s^{-1})
Level 1	190	1200
Level 2	280	1600
Level 3	370	2000

Additionally, scanning strategy and contour scan are canceled to investigate the effects of only laser power and scanning speed on microstructure features. Laser scanning is the same for each layer of the specimen and continues uninterrupted from one edge to another edge (see Figure 1).

Operations of positioning the specimens and assigning process parameters are carried out using Materialise Magics software. After the manufacturing process, specimens are separated from the build table using a Mitsubishi Electric MV2400R wire erosion machine.

Volumetric energy density is used to determine the energy input. The equation of the energy density used in the study is given in Equation (1).

$$\mathrm{ED} = \frac{P}{Vht} \tag{1}$$

Table 2: Other process parameters.

Layer thickness (μm)	Hatch distance (μm)	Spot size (μm)	Pre-heating temperature (°C)
25	112	120	200

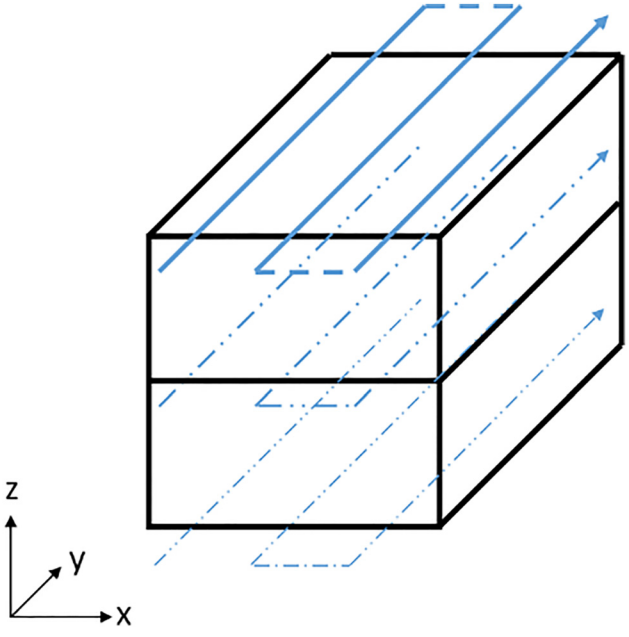

Figure 1: Laser scanning path used in manufacturing.

with ED: energy density, P: laser power, V: scanning speed, h: hatch distance and t: layer thickness. The energy density values of the manufactured specimens are listed in Table 3, and it is calculated that the energy density variates between 33.93 and 110.12 J mm^{-3}.

After the specimens are prepared, firstly the etching process with Keller's reagent is applied to the as-built specimens. Then, the microstructure images are obtained to determine the dimensions of Si precipitates, eutectic cells and melt pools as discussed in the subsequent sections.

2.2 Microstructure and mechanical properties characterization

Cell size

The microstructure images are obtained with different magnification rates using Quanta 400 F Field Emission scanning electron microscopy (SEM) from the inside of the melt pool of the specimens produced with different process parameters. Figure 2 shows the microstructure images corresponding to Specimen 8. The images obtained with 60 k magnification rate are used to measure cell size by the image processing method.

Si precipitate

The microstructure images are obtained using FEI Nova NanoLab 600i SEM with a focused ion beam (FIB) from the inside of the melt pool of the specimens produced with different process parameters. In addition, the dimensions of Si precipitates are measured using the measurement tool of the microscope. The microstructure images and measured Si precipitates with the microscope tool are shown in Figure 3, which corresponds to Specimen 6.

Table 3: Process parameters and energy density values of the specimens.

Specimen ID	Laser power (W)	Scanning speed (mm s^{-1})	Energy density (J mm^{-3})
1	190	1200	56.55
2	280	1200	83.33
3	370	1200	110.12
4	190	1600	42.41
5	280	1600	62.50
6	370	1600	82.59
7	190	2000	33.93
8	280	2000	50.00
9	370	2000	66.07

Melt pool

Melt pool shape and size can change due to the process parameters and thermal effects. The melt pool is assumed hemispherical when the width/depth ratio is below 0.5. However, when the ratio is above 0.5 the melt pool takes an elliptical shape due to the key-hole mode resulting defects within the structures [25]. Melt pool width derived from the Rosenthal model can be formulated as:

$$W \approx \sqrt{\frac{8}{\pi e}\frac{\alpha P}{\rho C_p V (T_m - T_0)}} \tag{2}$$

with ρ: density, T_m: melting temperature, T_0: temperature far from the melt pool, α: absorption ratio, P: laser power and V: scanning speed [26].

The images of the top layer are obtained using Nikon MA100 optical microscope. Due to the hatch distance, the melt pools intersect with each other; hence, it is not possible to directly measure the width of the melt pool for multi-bead specimens. Therefore, melt pool depth is measured and then melt pool width is calculated by assuming the shape as hemispherical. Filtering and depth measurement processes are completed by using optical microscope images obtained at 100, 200 and 500× magnification ratios for each specimen in ImageJ software (Figure 4).

Nano-indentation

In this study, NI hardness tests are carried out at 10 points by moving on a single axis (along the width) while remaining in the melt pool. Before the tests, specimens are ground with 180, 240, 320, 400, 600 and 1000-grade grinding papers, respectively. Then, the polishing operation is completed with a Struers polishing machine. NI tests are performed with a maximum load of 20 mN and a loading/unloading of 40 mN/s according to ASTM E2546-07 standard using CSM Instrument TTX-NHT NI machine with a Berkovich diamond indentor [27]. Finally, the Oliver–Pharr method is used to calculate the hardness and elastic modulus of the specimens by using force-displacement curves as inputs [28].

Hardness-yield strength relation

In the literature, there are many studies related to establishing a correlation between the hardness and strength of the structure for Al alloys [29–32]. The hardness-strength relation developed by expanding Tabor's study [33] is specified in Equation (3).

$$\sigma_y = \left(\frac{H}{3}\right)B^n \tag{3}$$

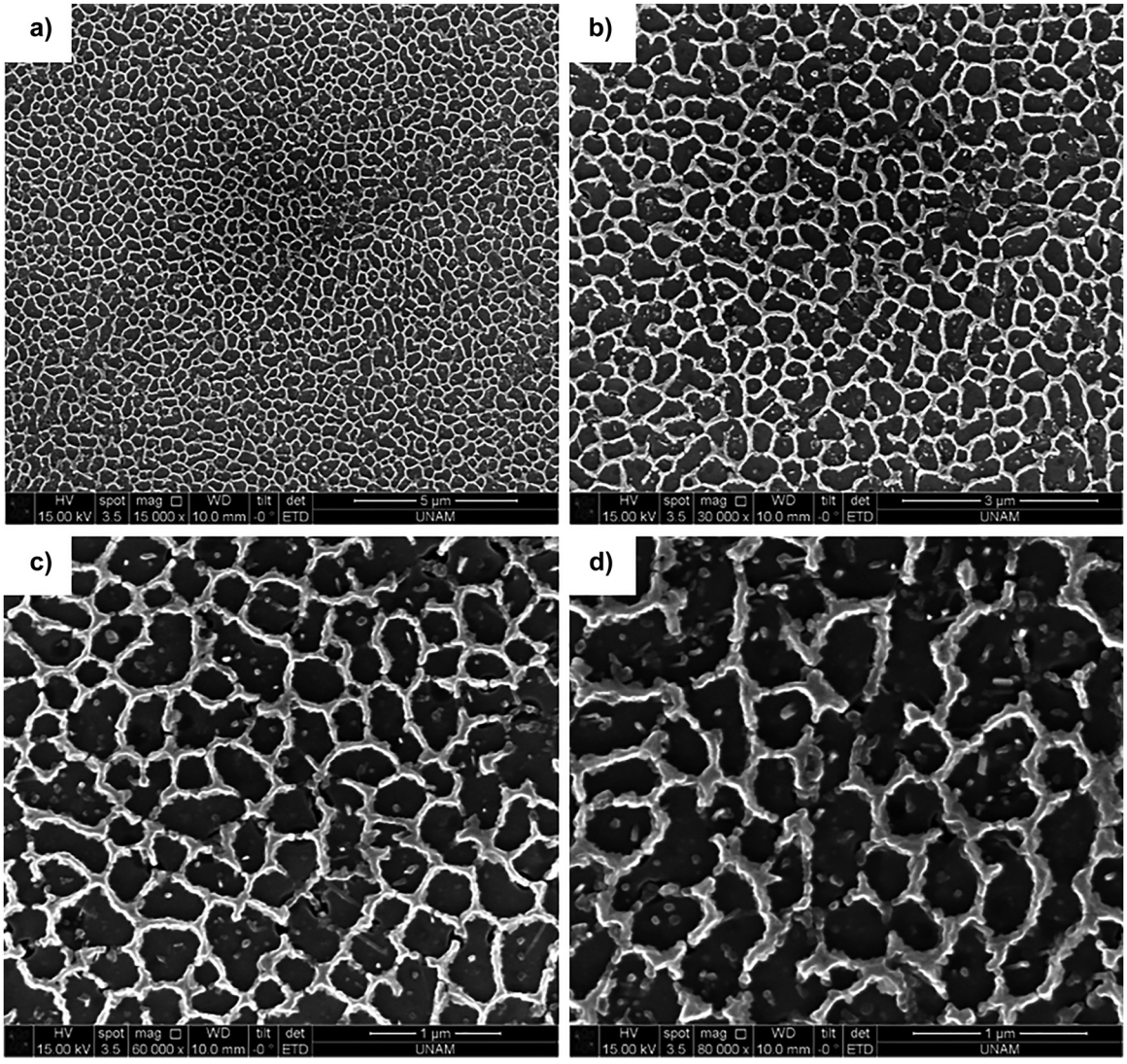

Figure 2: Morphology of cell structures in as-built AlSi10Mg obtained with SEM at different magnifications, a) 15kX, b) 30kX, c) 60kX and d) 80kX.

with H: vickers hardness (MPa), B: material constant obtained by experimental studies and n: strain hardening coefficient.

In this study, n and B are taken as 0.252 and 0.1, respectively, for yield strength calculations [21].

3 Results and discussion

3.1 Results of microstructure and mechanical properties

Cell size results

Measured eutectic cell size results with respect to laser power and scanning speed are given in Table 4. It is seen that cell size decreases when the laser power is kept constant and the scanning speed is increased. It is also seen that cell size increases as laser power increases and the scanning speed is kept constant. When the results are evaluated, it is seen that some points are out of the general cell size trend, which might be due to measurement error. It is also observed that the trends are consistent with the experimental studies in the literature, which have shown that as the laser power increases, the average cell size enlarges and the relation between scanning speed and cell size is inversely proportional [11, 12, 34, 35].

In AlSi10Mg structures produced at high solidification rates by melting with laser, Si accumulates at the Al cell boundaries [36–38]. The cooling rate affecting the microstructures is obtained using the Rosenthal model as stated in Equation (4) [36].

$$\dot{T} = 2\pi k\,(T_s - T_0)\,(T_l - T_0)\,\frac{v}{Q_p} \tag{4}$$

with $\dot{T}$: cooling rate, T_s and T_l: solidus and liquidus temperature, respectively, T_0: plate temperature, v: scanning speed and Q_p: absorbed laser power.

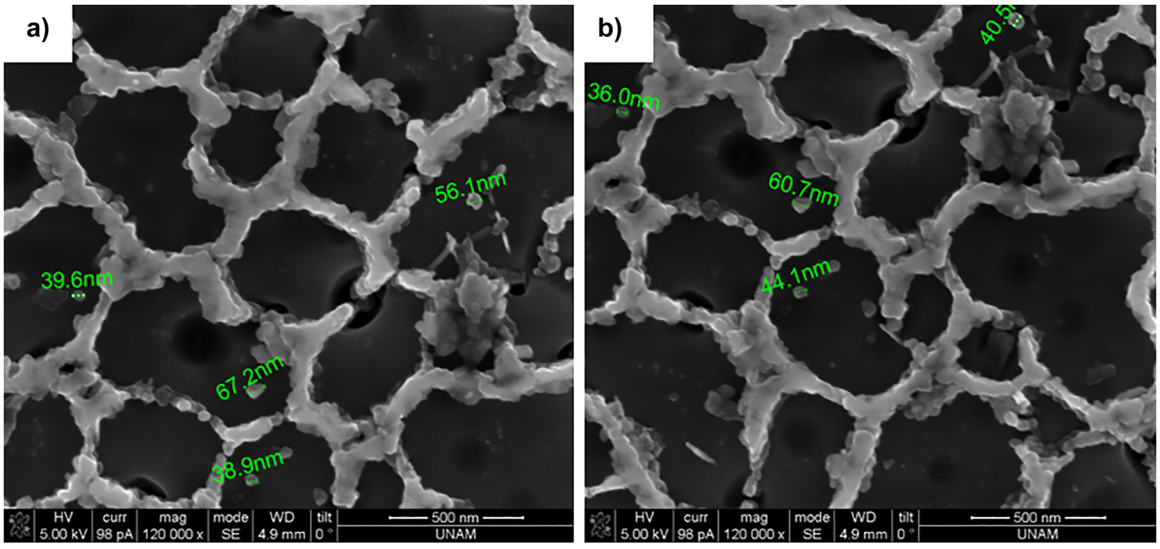

Figure 3: The morphology of cell structures and measured Si precipitates of Specimen 6 by microscope tool from different positions, a) position 1, b) position 2.

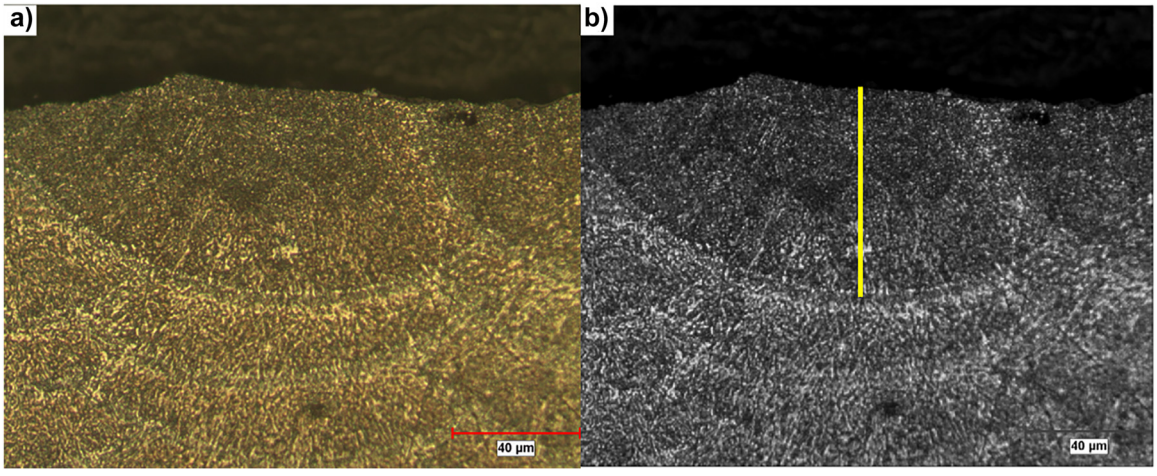

Figure 4: The image taken from the top layer of Specimen 4 with 500x, a) raw image, b) filtering the image and measurement of melt pool depth by drawing a line.

Table 4: Cell size results of the specimens.

Cell size (µm)	Laser power (W)	Scanning speed (mm s^{-1})	Energy density (J mm^{-3})
0.8069	190	1200	56.55
1.1040	280	1200	83.33
1.0490	370	1200	110.12
0.4187	190	1600	42.41
0.6572	280	1600	62.50
1.0280	370	1600	82.59
0.5513	190	2000	33.93
0.5200	280	2000	50.00
0.7468	370	2000	66.07

Equation (4) states that the microstructure can be manipulated by changing the heat input (Q_p/v). Equation (5) is used to calculate the cell size of Al alloys produced at high cooling rates.

$$\lambda = a_1\left(\dot{T}\right)^{-n} \tag{5}$$

with λ: dimension of the cell size, a_1 and n: curve fitting coefficients.

In this study, an exponential equation is used to obtain a relation between cooling rate and cell size. In the equation given in Table 5, α is the absorption ratio (0.35 for L-PBF AlSi10Mg) [36], P is the laser power and v is the scanning

speed. The equation format, coefficients of the equation and the curve fitting accuracy level determining by normalized root mean square error (NRMSE) are listed in Table 5. It is seen that the NRMSE is 18%, where NRMSE is calculated from

$$\mathrm{NRMSE} = \frac{\sqrt{\frac{1}{n}\sum_{i=1}^{n}(f_i - y_i)^2}}{(y_{\max} - y_{\min})} \tag{6}$$

with n: sampling point, f_i: estimated result, y_i: experimental result, $y_{\max}$ and $y_{\min}$: maximum and minimum experimental results, respectively.

Since the features and cell sizes change according to the position in the microstructure and it is not possible to take images from the same location in all specimens, the calculated NRMSE value is considered to be sufficient. In addition, the isometric view and contour results of the fitted equation are given in Figure 5. According to the studies in the literature, cell size is proportional to the energy input [36, 39–41]. In this study, similar to the studies in the literature, it is found that cell size increases with increasing energy density or energy input.

Si precipitate results

The thermal conditions related to the process parameters affect the precipitate density, number and size. It is determined that precipitate size decreases and the number of precipitates increases as the cooling rate increases [42]. Table 6 shows that as the laser power increases the Si precipitate diameter also increases, whereas as the scanning speed increases the Si precipitate diameter reduces. In addition, since the concepts of energy density and cooling rate are inversely proportional to each other, it is expected that the precipitate diameter, which is inversely proportional to the cooling rate, is directly proportional to the energy density. Table 6 also shows that the Si precipitate diameter increases with the increase in energy density, as expected.

In the existing studies, exponential functions are used when establishing the relationship between the cooling rate and Si precipitates [42]. Therefore, an exponential function is used to calculate the Si precipitate diameter in the study. The equation format, the coefficients of the equation and the curve-fitting accuracy level are listed in Table 7. The NRMSE value is found to be 6.2%, which is considered to be acceptable. In addition, the isometric view and contour results of the fitted function are given in Figure 6.

Table 5: Details of fitted eutectic cell size equation.

Equation name	Equation format	a_3	a_4	R^2	R^2_{adj}	NRMSE
Relation of cell size and process parameters	$f(P,v) = a_3\left(\frac{aP}{v}\right)^{a^4}$	0.0067	0.788	0.78	0.75	0.18

Nano-indentation test results

In the literature, the hardness value of the as-built AlSi10Mg material processed by L-PBF is measured in the range of 1.52–2.10 GPa [9, 43, 44]. The hardness values obtained by the NI hardness test of the specimens produced with different process parameters are given in Table 8. It is observed that the hardness values vary between 1.56 and 1.84 GPa, and it is considered to be compatible with the results of the hardness measurements in the literature.

The hardness value of as-built AlSi10Mg is proportional to the scanning speed and inversely proportional to the laser power [13]. Additionally, the hardness value of additively manufactured Al Alloys decreases with increasing energy density [45, 46]. Figure 7 shows that the lowest hardness value is observed in the specimen with the highest energy density, while the highest hardness value is observed in one of the specimens with the lowest energy density. In addition, when an exponential function is fitted using the results, NRMSE value is calculated as 11.6%.

In this study, the yield strength is estimated by using Equation (3) with n = 0.252 and B = 0.1, based on using the hardness-strength relation. When the results of as-built specimens manufactured with different process parameters are investigated, it was found that the yield strength is proportional to the scanning speed and inversely proportional to the laser power [13, 47]. Figure 8 shows for this study that the yield strength increases with increasing the scanning speed and decreases with decreasing laser power, as expected.

Melt pool area results

In this study, the melt pool area is measured by assuming a semi-circular melt pool shape. An exponential function is used to obtain a relationship between the cooling rate and melt pool area [12]. The equation format, the coefficients of the equation and the curve-fitting accuracy level are listed in Table 9. The NRMSE for the melt pool area estimation is 12.5%. In addition, the isometric view and contour results of the fitted function are given in Figure 9. It is seen that the melt pool area is proportional to the laser power and inversely proportional to the scanning speed as well as melt pool area is increasing with energy input. These trends, which are observed according to changes in process parameters and energy density, are compatible with the Rosenthal equation (Equation (2)).

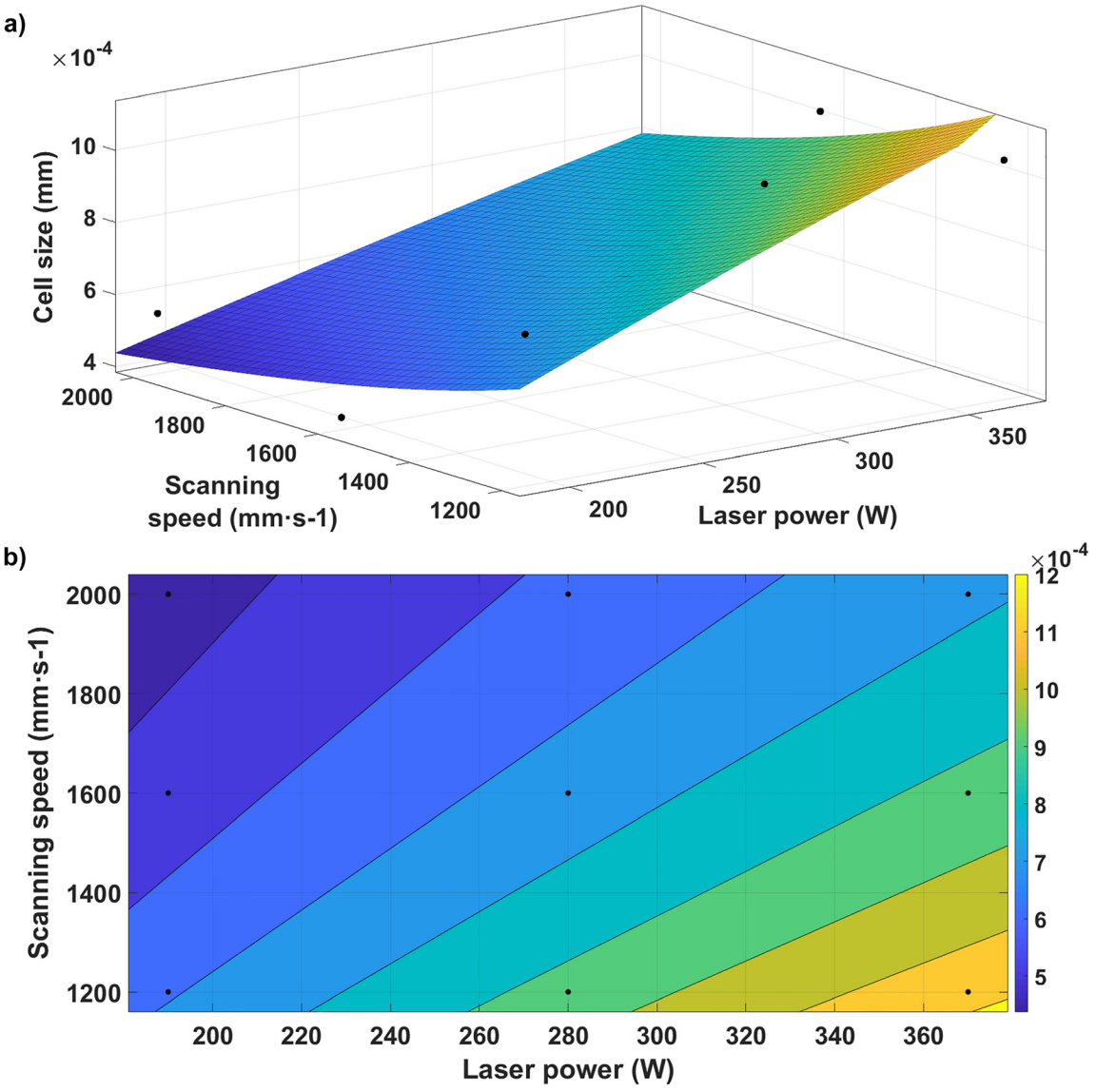

Figure 5: The images of the fitted eutectic cell size function, a) isometric, b) contour.

Table 6: Si precipitate diameter results of the specimens.

Si precipitate diameter (nm)	Laser power (W)	Scanning speed (mm s^{-1})	Energy density (J mm^{-3})
47.99	190	1200	56.55
59.97	280	1200	83.33
65.83	370	1200	110.12
42.02	190	1600	42.41
51.62	280	1600	62.50
56.49	370	1600	82.59
32.81	190	2000	33.93
41.74	280	2000	50.00
51.27	370	2000	66.07

3.2 Strengthening mechanisms

Hall-Petch (H-P) strengthening mechanism

According to the Hall–Petch equation, the mechanical properties of polycrystal metal materials depend on internal friction stress and grain size in microstructure (Equation (7)).

$$\sigma = \frac{k}{\sqrt{d}} \tag{7}$$

with σ_0: resistance to dislocation motion, k: strengthening coefficient and d: grain size.

Table 7: Details of fitted Si precipitate diameter equation.

Equation name	Equation format	a_5	a_6	R^2	R^2_{adj}	NRMSE
Relation of Si precipitate diameter and process parameters	$f(P,v) = a_5\left(\frac{aP}{v}\right)^{a_6}$	226.6	0.5445	0.96	0.96	0.062

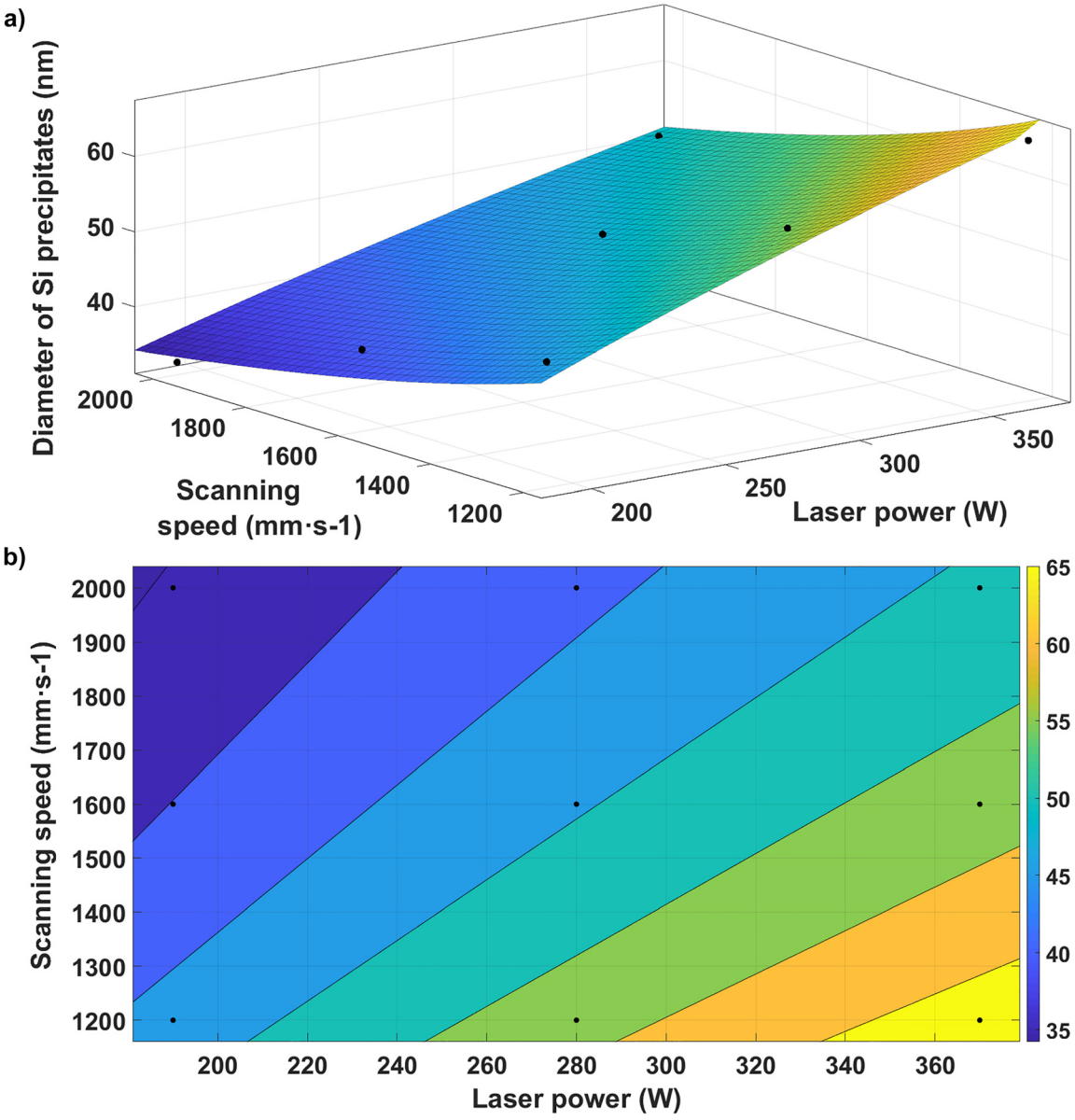

Figure 6: The images of the fitted Si precipitate diameter function, a) isometric, b) contour.

The eutectic cell size is used to calculate the H-P strengthening mechanism of AlSi10Mg material manufactured with AM [22, 48]. When the cell size equation obtained in Section 3.1 is integrated into Equation (7), the H-P mechanism becomes a function of the process parameters (see Equation (8)), where k is taken as 0.04 MPa $m^{1/2}$ [49].

$$\sigma_{\text{H-P}} = \frac{k}{\sqrt{d_{\text{cell size}}}} = \frac{k}{\sqrt{0.0067\left(\frac{aP}{v}\right)^{0.788}}} \tag{8}$$

The H-P strength values calculated using experimental results and Equation (8) are listed in Table 10, respectively. It

Table 8: Hardness values of the specimens.

Hardness (HV)	Hardness (GPa)	Laser power (W)	Scanning speed (mm s^{-1})
152.97 ± 6.14	1.652	190	1200
149.88 ± 7.92	1.618	280	1200
144.97 ± 6.58	1.565	370	1200
170.76 ± 9.92	1.847	190	1600
158.14 ± 7.43	1.708	280	1600
149.52 ± 5.53	1.614	370	1600
168.50 ± 10.65	1.819	190	2000
164.33 ± 5.41	1.775	280	2000
157.10 ± 6.37	1.696	370	2000

is observed that the difference is approximately in the range of 2–12%.

Orowan strengthening mechanism

AlSi10Mg structures fabricated with L-PBF have high strength due to the boundaries of eutectic cells and Si precipitates that prevent dislocation movement during deformation [19]. The Orowan strength of Al-Si alloys is calculated by Equation (9) [20].

$$\sigma_{\text{Orowan}} = \frac{\varphi \text{Gb}}{d_{\text{Si}}}\left(\frac{6V_{\text{Si}}}{\pi}\right)^{1/3} \tag{9}$$

with G: shear modulus (26.5 GPa for Al matrix), b: Burger's vector (0.286 nm for Al) [21], d_{Si}: diameter of Si precipitates, V_{Si}: volume fraction of Si precipitates (2.5%) [20] and φ: Material constant (0.4 for semi-coherent Si precipitates) [50].

Table 9: Details of fitted melt pool area equation.

Equation name	Equation format	a_3	a_4	R^2	R^2_{adj}	NRMSE
Relation of melt pool area and process parameters	$f(P,v) = a_1\left(\frac{aP}{v}\right)^{a^2}$	1.128	1.544	0.92	0.91	0.125

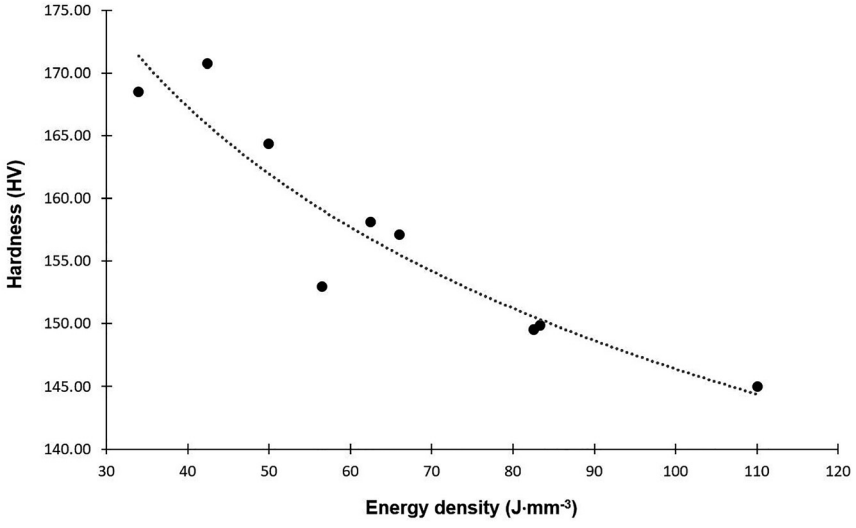

Figure 7: Change of hardness with respect to energy density.

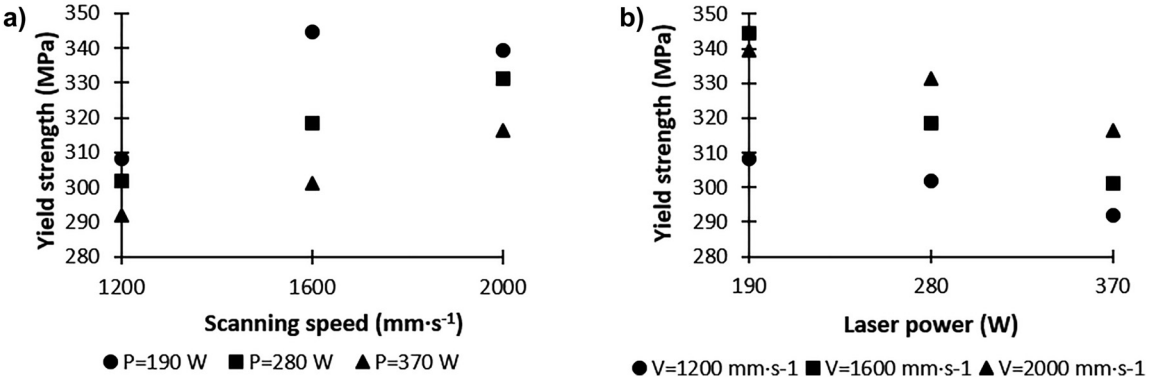

Figure 8: Change of yield strength with respect to a) scanning speed and b) laser power.

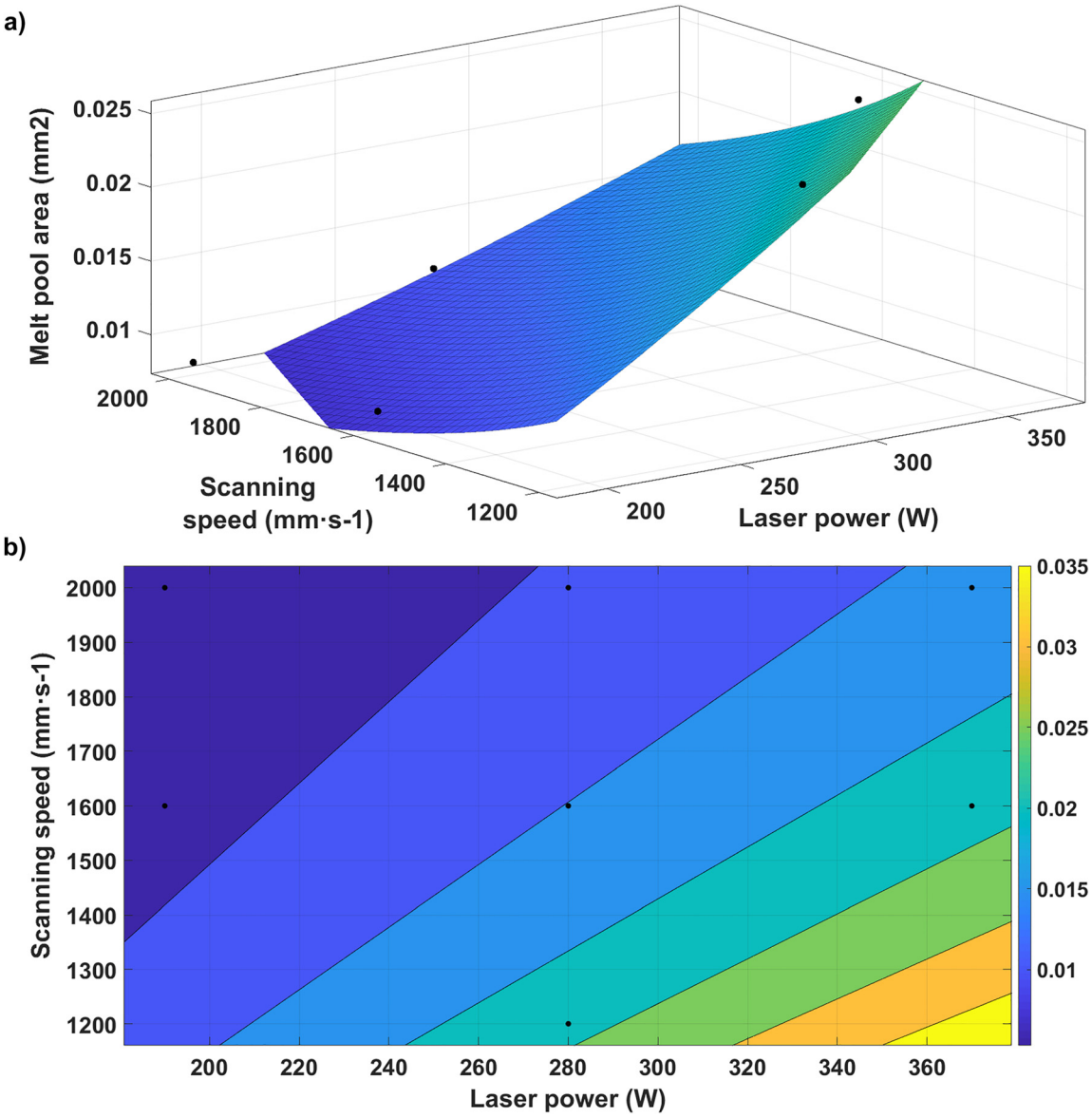

Figure 9: The images of the fitted melt pool area function, a) isometric, b) contour.

Table 10: Calculated H-P strengths.

H-P strength (MPa) (experimental)	H-P strength (MPa) (Equation (8))	Difference (%)	Energy density (J mm^{-3})
44.53	48.31	8.49	56.55
38.07	41.46	8.92	83.33
39.05	37.15	4.87	110.12
61.82	54.11	12.47	42.41
49.34	46.44	5.88	62.50
39.45	41.61	5.47	82.59
53.87	59.08	9.67	33.93
55.47	50.71	8.58	50.00
46.29	45.44	1.84	66.07

When the cell size equation obtained in Section 3.2 is integrated into Equation (9), the Orowan strengthening mechanism becomes a function of the process parameters (see Equation (10)).

$$\sigma_{\text{Orowan}}(P, v) = \frac{\varphi \text{Gb}}{226.6\left(\frac{aP}{v}\right)^{0.5445}}\left(\frac{6V_{\text{Si}}}{\pi}\right)^{1/3} \tag{10}$$

The Orowan strength values calculated using experimental results and Equation (10) are listed in Table 11, respectively. It is seen that the maximum difference between the two calculated results is 7.65%.

Table 11: Calculated Orowan strengths.

Orowan strength (MPa) (experimental)	Orowan strength (MPa) (Equation (10))	Difference (%)	Energy density (J mm^{-3})
100.59	102.88	2.28	56.55
80.50	83.30	3.48	83.33
73.33	71.57	2.40	110.12
114.87	120.32	4.75	42.41
93.52	97.42	4.17	62.50
85.46	83.70	2.05	82.59
147.12	135.87	7.65	33.93
115.66	110.01	4.89	50.00
94.16	94.52	0.38	66.07

Dislocation hardening mechanism

In this study, the dislocation hardening mechanism is calculated using Equation (11) [22].

$$\sigma_{\text{dislocation}} = \beta \text{MGb}\sqrt{\rho_d} \tag{11}$$

Table 12: Comparison of experimentally and parametrically calculated yield strength of AlSi10Mg.

Specimen ID	NI test results (MPa)	Estimated results (MPa)	Difference (%)	Energy density (J mm^{-3})
1	308.19	292.04	5.24	56.55
2	301.97	265.61	12.04	83.33
3	292.07	249.57	14.55	110.12
4	344.58	315.27	8.51	42.41
5	318.59	284.71	10.64	62.50
6	301.23	266.16	11.64	82.59
7	339.48	335.80	1.09	33.93
8	331.27	301.57	8.97	50.00
9	316.51	280.80	11.28	66.07

with β: strengthening coefficient (0.25 for structures with multiple slip systems during quasi-stationary deformation) [51], M: Taylor factor (3.06 for FCC crystal materials) [21] and ρ_d: dislocation density which is affected by process parameters and thermal behavior.

The ρ_d term is taken as 1.41×10^{14} m^{-2} for as-built AlSi10Mg produced by L-PBF [22]. In addition, steady-state deformation is assumed since the loading rate is kept constant during the NI tests. In this study, dislocation hardening is constant and calculated as 68.85 MPa using Equation (11).

3.3 Comparison of NI test results and estimated results

In the study, strengthening mechanisms of the yield strength model are obtained as a function of the process parameters by using experimental results. Measured eutectic cell size and Si precipitate diameter are used in H-P and Orowan mechanisms, respectively. Thus, the yield strength model of AlSi10Mg material becomes a function of the laser power and scanning speed. In the model, σ_0 term is independent of the process parameters (72 MPa for Al) and dislocation hardening is taken as constant. When the equations obtained by curve fitting using experimental results are integrated into the yield strength model of AlSi10Mg, Equation (12) is obtained.

$$\begin{aligned}\sigma(P,v) &= \sigma_0 + \sigma_{\text{H-P}}(P,v) + \sigma_{\text{Orowan}}(P,v) + \sigma_{\text{dislocation}} \\ &= \sigma_0 + \frac{k}{\sqrt{0.0067\left(\frac{\alpha P}{v}\right)^{0.788}}} \\ &\quad + \frac{\varphi \text{Gb}}{226.6\left(\frac{\alpha P}{v}\right)^{0.5445}}\left(\frac{6V_{\text{Si}}}{\pi}\right)^{1/3} + \beta \text{MGb}\sqrt{\rho_d}\end{aligned} \tag{12}$$

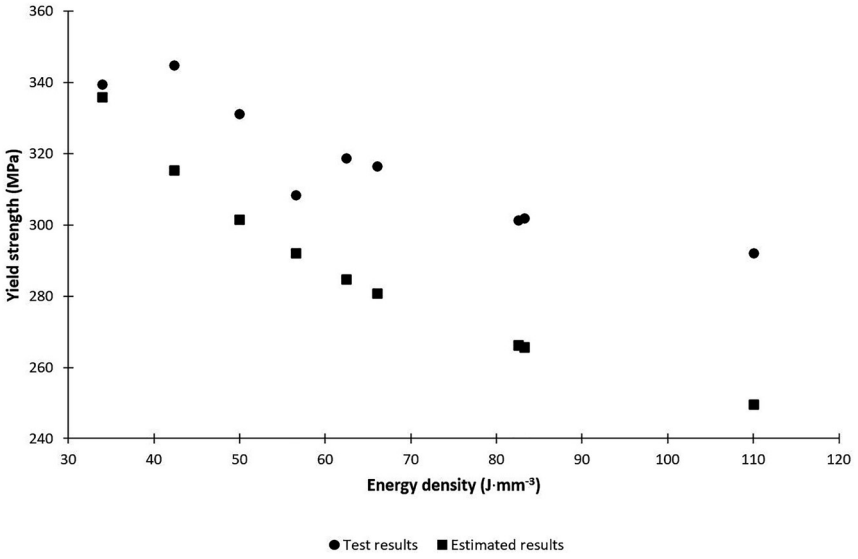

Figure 10: Estimated and measured yield strengths according to energy densities.

Table 12 shows the yield strength values of the as-built AlSi10Mg specimens manufactured with different process parameters calculated using Equation (12). The comparison of the yield strength values estimated with Equation (12) and those measured in NI tests shows that the difference between the two values varies according to energy density, and the differences range between 1.09 and 14.55%. It is evaluated that the difference is due to experimental measurement errors as well as the assumption of the dislocation hardening mechanism as constant. In addition, the estimated yield strength values and test results corresponding to different energy densities are shown in Figure 10.

4 Conclusions

In this study, nine different process parameter combinations were determined by FFD design of experiments, and the specimens were manufactured with L-PBF to investigate the effects of process parameters on the microstructural features, strengthening mechanisms and mechanical properties. Microstructural features of as-built AlSi10Mg material were determined as eutectic cell size and Si precipitates formed due to rapid cooling. Therefore, eutectic cell size and diameter of Si precipitates of manufactured specimens were measured using microstructure images obtained by SEM as well as image processing methods. Moreover, the hardness values of specimens were measured with NI tests to calculate the yield strength. The conversion of the hardness values measured inside the melt pool to the yield strength was assessed by using the hardness-strength relationship. The equations for eutectic cell size and Si precipitate diameter as a function of process parameters were obtained using the experimental results. The parametric yield strength model of AlSi10Mg material depending on the process parameters was obtained by integrating the generated equations into the related strengthening mechanisms. Finally, a comparison was performed between the parametric yield strength model and experimental results. Additionally, melt pools were measured using images taken from the top layers of the specimens, and the melt pool area equation as a function of process parameters was fitted using experimental results. From the results of this study, the following conclusions were drawn:

- The melt pool area of the specimen increased with increasing laser power and decreased with increasing scanning speed. The NRMSE value of the fitted melt pool function was calculated as 0.125.
- Eutectic cell size was proportional to the laser power and inversely proportional to the scanning speed. The error was observed to vary between 2% and 12% when the cell size equation generated as a function of process parameters was integrated into the H-P strengthening mechanism.
- It was observed that the diameter of Si precipitates was enlarged as the energy density increased. When the measured results were compared with the estimated results for the Orowan mechanism, the maximum difference was approximately 7%.
- According to the NI results, it was seen that the hardness value was inversely proportional to the energy density and proportional to the cooling rate.
- The Orowan mechanism, which was affected by Si precipitates formed due to high cooling rates, was determined as the most dominant strengthening mechanism of as-built AlSi10Mg material manufactured with L-PBF. In addition, it was observed that the H-P strengthening mechanism was the sub-mechanism that contributed the least effect on the yield strength.
- When the results of the parametric yield strength model were compared with the yield strength results obtained from the NI test results, it was found that the generated equation predicted the yield strength of as-built AlSi10Mg material with a deviation between 1% and 14% for different process parameters variations.

In addition to this study, the dislocation density could be measured and the dislocation hardening mechanism could be integrated into the developed yield strength equation to reduce the margin of error by obtaining it as a function of the process parameters. Moreover, the parameters such as hatch distance, scanning strategy and pre-heating temperature affecting microstructure and mechanical properties could be investigated and added to the developed model. Finally, the developed model could be tested by investigating specimens manufactured with different parameters, and compared with the studies whose parameters are given in the literature.

Acknowledgement: The authors acknowledge the support of EKTAM for manufacturing specimens, UNAM for SEM and nano-indentation, Dr. Gülten Kafadar for her help in SEM and nano-indentation measurements and Additive Manufacturing Technology Center of Turkish Aerospace Industries for supporting the study.
Author contributions: All the authors have accepted responsibility for the entire content of this submitted manuscript and approved submission.

Research funding: This study is a part of the project (# 5189901) supported by The Scientific and Technological Research Council of Turkey (TÜBİTAK) under the Frontier R&D Laboratory Support Programme and performed in Turkish Aerospace Industries Inc. This work was funded by The Scientific and Technological Research Council of Turkey (TÜBİTAK) (5189901)

Conflict of interest statement: The authors declare no conflicts of interest regarding this article.

References

[1] I. Gibson, D. W. Rosen, and B. Stucker, *Additive Manufacturing Technologies*, New York, NY, Springer, 2010.

[2] B. Aslan and A. R. Yıldız, "Optimum design of automobile components using lattice structures for additive manufacturing," *Mater. Test.*, vol. 62, no. 6, pp. 633–639, 2020, https://doi.org/10.3139/120.111527.

[3] İ. Gökdağ, O. İzgü, A. Dağkolu, A. A. Tanrıkulu, and E. Acar, "Design optimization and validation for additive manufacturing: a satellite bracket application," *Struct. Multidiscip. Optim.*, vol. 65, no. 8, p. 237, 2022, https://doi.org/10.1007/s00158-022-03345-3.

[4] İ. Gökdağ and E. Acar, "Application of a modular topology optimization framework to an aerospace bracket design," *Mater. Test.*, vol. 64, no. 7, pp. 1090–1102, 2022, https://doi.org/10.1515/mt-2021-2148.

[5] T. Sonar, V. Balasubramanian, S. Malarvizhi, A. Nagar, T. Venkateswaran, and D. Sivakumar, "Microstructural characteristics and tensile properties of gas tungsten constricted arc (GTCA) welded Inconel 718 superalloy sheets for aeroengine components," *Mater. Test.*, vol. 62, no. 11, pp. 1099–1108, 2020, https://doi.org/10.3139/120.111576.

[6] A. Ramaswamy, S. Malarvizhi, and V. Balasubramanian, "Post-weld heat treatment effects on the tensile properties of cold metal arc welded AA 6061-T6 aluminum joints," *Mater. Test.*, vol. 62, no. 1, pp. 69–76, 2020, https://doi.org/10.3139/120.111454.

[7] S. Y. Ahn, J. Moon, Y. T. Choi, et al., "A precipitation-hardened AlSi10Mg alloy fabricated using selective laser melting," *Mater. Sci. Eng. A*, vol. 844, no. June, p. 143164, 2022, https://doi.org/10.1016/j.msea.2022.143164.

[8] C. D. Clement, J. Masson, and A. S. Kabir, "Effects of heat treatment on microstructure and mechanical properties of AlSi10Mg fabricated by selective laser melting process," *J. Manuf. Mater. Process.*, vol. 6, no. 3, 2022, https://doi.org/10.3390/jmmp6030052.

[9] J. Delahaye, J. T. Tchuindjang, J. Lecomte-Beckers, O. Rigo, A. M. Habraken, and A. Mertens, "Influence of Si precipitates on fracture mechanisms of AlSi10Mg parts processed by selective laser melting," *Acta Mater.*, vol. 175, pp. 160–170, 2019, https://doi.org/10.1016/j.actamat.2019.06.013.

[10] A. Lutz, L. Huber, and C. Emmelmann, "Strain-rate dependent material properties of selective laser melted AlSi10Mg and AlSi3.5Mg2.5," *Mater. Test.*, vol. 62, no. 6, pp. 573–583, 2020, https://doi.org/10.3139/120.111518.

[11] H. Hyer, L. Zhou, S. Park, et al., "Understanding the laser powder bed fusion of AlSi10Mg alloy," *Metallogr. Microstruct. Anal.*, vol. 9, no. 4, pp. 484–502, 2020, https://doi.org/10.1007/s13632-020-00659-w.

[12] S. P. Narra, L. Scime, and J. Beuth, "Integrated control of melt pool geometry and microstructure in laser powder bed fusion of AlSi10Mg," *Metall. Mater. Trans. A Phys. Metall. Mater. Sci.*, vol. 49, no. 10, pp. 5097–5106, 2018, https://doi.org/10.1007/s11661-018-4804-z.

[13] A. H. Maamoun, Y. F. Xue, M. A. Elbestawi, and S. C. Veldhuis, "The effect of selective laser melting process parameters on the microstructure and mechanical properties of Al6061 and AlSi10Mg alloys," *Materials*, vol. 12, no. 1, p. 12, 2018. https://doi.org/10.3390/ma12010012.

[14] H. Wu, Y. Ren, J. Ren, et al., "Selective laser melted AlSi10Mg alloy under melting mode transition: microstructure evolution, nanomechanical behaviors and tensile properties," *J. Alloys Compd.*, vol. 873, p. 159823, 2021, https://doi.org/10.1016/j.jallcom.2021.159823.

[15] Y. Geng, H. Tang, J. Xu, et al., "Influence of process parameters and aging treatment on the microstructure and mechanical properties of AlSi8Mg3 alloy fabricated by selective laser melting," *Int. J. Miner. Metall. Mater.*, vol. 29, no. 9, pp. 1770–1779, 2022, https://doi.org/10.1007/s12613-022-2530-4.

[16] W. Pan, Z. Ye, Y. Zhang, Y. Liu, B. Liang, and Z. Zhai, "Research on microstructure and properties of AlSi10Mg fabricated by selective laser melting," *Materials*, vol. 15, no. 7, p. 2528, 2022. https://doi.org/10.3390/ma15072528.

[17] D. Gu, X. Shi, R. Poprawe, D. Bourell, R. Setchi, and J. Zhu, "Material-structure-performance integrated laser-metal additive manufacturing," *Science*, vol. 372, p. eabg1487, 2021, https://doi.org/10.1126/science.abg1487.

[18] Q. Liu, H. Wu, M. J. Paul, et al., "Machine-learning assisted laser powder bed fusion process optimization for AlSi10Mg: new microstructure description indices and fracture mechanisms," *Acta Mater.*, vol. 201, pp. 316–328, 2020, https://doi.org/10.1016/j.actamat.2020.10.010.

[19] J. Wu, X. Q. Wang, W. Wang, M. M. Attallah, and M. H. Loretto, "Microstructure and strength of selectively laser melted AlSi10Mg," *Acta Mater.*, vol. 117, pp. 311–320, 2016, https://doi.org/10.1016/j.actamat.2016.07.012.

[20] X. P. Li, G. Ji, Z. Chen, et al., "Selective laser melting of nano-TiB2 decorated AlSi10Mg alloy with high fracture strength and ductility," *Acta Mater.*, vol. 129, pp. 183–193, 2017, https://doi.org/10.1016/j.actamat.2017.02.062.

[21] B. Chen, S. Moon, X. Yao, et al., "Strength and strain hardening of a selective laser melted AlSi10Mg alloy," *Scr. Mater.*, vol. 141, pp. 45–49, 2017, https://doi.org/10.1016/j.scriptamat.2017.07.025.

[22] A. Hadadzadeh, C. Baxter, B. S. Amirkhiz, and M. Mohammadi, "Strengthening mechanisms in direct metal laser sintered AlSi10Mg: comparison between virgin and recycled powders," *Addit. Manuf.*, vol. 23, no. July, pp. 108–120, 2018, https://doi.org/10.1016/j.addma.2018.07.014.

[23] A. Hadadzadeh, B. S. Amirkhiz, and M. Mohammadi, "Contribution of Mg2Si precipitates to the strength of direct metal laser sintered AlSi10Mg," *Mater. Sci. Eng. A*, vol. 739, pp. 295–300, 2019. https://doi.org/10.1016/j.msea.2018.10.055.

[24] A. Hadadzadeh, B. S. Amirkhiz, B. Langelier, J. Li, and M. Mohammadi, "Microstructural consistency in the additive manufactured metallic materials: a study on the laser powder fusion of AlSi10Mg," *Addit. Manuf.*, vol. 46, p. 102166, 2021, https://doi.org/10.1016/j.addma.2021.102166.

[25] J. Metelkova, Y. Kinds, K. Kempen, C. de Formanoir, A. Witvrouw, and B. Van Hooreweder, "On the influence of laser defocusing in Selective Laser Melting of 316L," *Addit. Manuf.*, vol. 23, no. August, pp. 161–169, 2018, https://doi.org/10.1016/j.addma.2018.08.006.

[26] M. Tang, P. C. Pistorius, and J. L. Beuth, "Prediction of lack-of-fusion porosity for powder bed fusion," *Addit. Manuf.*, vol. 14, pp. 39–48, 2017, https://doi.org/10.1016/j.addma.2016.12.001.

[27] ASTM International. E2546-07, *Standard Practice for Instrumented Indentation Testing*, West Conshohocken, PA, ASTM International, 2007.
[28] W. C. Oliver and G. M. Pharr, "An improved technique for determining hardness and elastic modulus using load and displacement sensing indentation experiments," *J. Mater. Res.*, vol. 7, no. 6, pp. 1564–1583, 1992, https://doi.org/10.1557/JMR.1992.1564.
[29] A. P. Sekhar, S. Nandy, K. K. Ray, and D. Das, "Hardness – yield strength relation of Al-Mg-Si alloys," *IOP Conf. Ser. Mater. Sci. Eng.*, vol. 338, no. 1, p. 12011, 2018. https://doi.org/10.1088/1757-899X/338/1/012011.
[30] F. Alghamdi, X. Song, A. Hadadzadeh, B. Shalchi-Amirkhiz, M. Mohammadi, and M. Haghshenas, "Post heat treatment of additive manufactured AlSi10Mg: on silicon morphology, texture and small-scale properties," *Mater. Sci. Eng. A*, vol. 783, p. 139296, 2020, https://doi.org/10.1016/j.msea.2020.139296.
[31] M. Tiryakioğlu, J. S. Robinson, M. A. Salazar-Guapuriche, Y. Y. Zhao, and P. D. Eason, "Hardness-strength relationships in the aluminum alloy 7010," *Mater. Sci. Eng. A*, vol. 631, no. April, pp. 196–200, 2015, https://doi.org/10.1016/j.msea.2015.02.049.
[32] J. R. Cahoon, W. H. Broughton, and A. R. Kutzak, "The determination of yield strength from hardness measurements," *Metall. Trans.*, vol. 2, no. 7, pp. 1979–1983, 1971, https://doi.org/10.1007/BF02913433.
[33] D. Tabor, *The Hardness of Metals*, Oxford, UK, Clarendon Press, 1951.
[34] P. Köhnen, M. Létang, M. Voshage, J. H. Schleifenbaum, and C. Haase, "Understanding the process-microstructure correlations for tailoring the mechanical properties of L-PBF produced austenitic advanced high strength steel," *Addit. Manuf.*, vol. 30, no. September, p. 100914, 2019, https://doi.org/10.1016/j.addma.2019.100914.
[35] J. Shao, G. Yu, X. He, S. Li, R. Chen, and Y. Zhao, "Grain size evolution under different cooling rate in laser additive manufacturing of superalloy," *Opt. Laser Technol.*, vol. 119, no. March, p. 105662, 2019, https://doi.org/10.1016/j.optlastec.2019.105662.
[36] M. Tang, P. C. Pistorius, S. Narra, and J. L. Beuth, "Rapid solidification: selective laser melting of AlSi10Mg," *JOM*, vol. 68, no. 3, pp. 960–966, 2016, https://doi.org/10.1007/s11837-015-1763-3.
[37] L. Thijs, K. Kempen, J.-P. Kruth, and J. Van Humbeeck, "Fine-structured aluminium products with controllable texture by selective laser melting of pre-alloyed AlSi10Mg powder," *Acta Mater.*, vol. 61, no. 5, pp. 1809–1819, 2013, https://doi.org/10.1016/j.actamat.2012.11.052.
[38] K. Kempen, L. Thijs, J. Van Humbeeck, and J.-P. Kruth, "Mechanical properties of AlSi10Mg produced by selective laser melting," *Phys. Procedia*, vol. 39, pp. 439–446, 2012, https://doi.org/10.1016/j.phpro.2012.10.059.
[39] H. Matyja, B. C. Giessen, and N. J. Grant, "The effect of cooling rate on the dendrite spacing in splat-cooled aluminium alloys," *J. Inst. Met.*, vol. 96, pp. 30–32, 1968.
[40] M. C. Flemings, *Solidification processing*, New York, N.Y., McGraw-Hill Book Company, 1974.
[41] V. S. Zolotorevsky, N. A. Belov, and M. V. Glazoff, *Casting Aluminum Alloys*, Oxford, Elsevier Science, 2007, p. 155 [Online]. Available at: http://www.sciencedirect.com/science/book/9780080453705.
[42] Z. Xu, S. Wang, H. Wang, H. Song, S. Li, and X. Chen, "Effect of cooling rate on microstructure and properties of twin-roll casting 6061 aluminum alloy sheet," *Metals*, vol. 10, no. 9, pp. 1–11, 2020, https://doi.org/10.3390/met10091168.
[43] N. T. Aboulkhair, I. Maskery, C. Tuck, I. Ashcroft, and N. M. Everitt, "The microstructure and mechanical properties of selectively laser melted AlSi10Mg: the effect of a conventional T6-like heat treatment," *Mater. Sci. Eng. A*, vol. 667, pp. 139–146, 2016, https://doi.org/10.1016/j.msea.2016.04.092.
[44] L. Zhuo, Z. Wang, H. Zhang, et al., "Effect of post-process heat treatment on microstructure and properties of selective laser melted AlSi10Mg alloy," *Mater. Lett.*, vol. 234, pp. 196–200, 2019, https://doi.org/10.1016/j.matlet.2018.09.109.
[45] M. A. Pekok, R. Setchi, M. Ryan, Q. Han, and D. Gu, "Effect of process parameters on the microstructure and mechanical properties of AA2024 fabricated using selective laser melting," *Int. J. Adv. Manuf. Technol.*, vol. 112, nos. 1–2, pp. 175–192, 2021, https://doi.org/10.1007/s00170-020-06346-y.
[46] M. Giovagnoli, G. Silvi, M. Merlin, and M. T. Di Giovanni, "Optimisation of process parameters for an additively manufactured AlSi10Mg alloy: limitations of the energy density-based approach on porosity and mechanical properties estimation," *Mater. Sci. Eng. A*, vol. 802, no. May 2020, p. 140613, 2021, https://doi.org/10.1016/j.msea.2020.140613.
[47] A. M. Khorasani, I. Gibson, U. S. Awan, and A. Ghaderi, "The effect of SLM process parameters on density, hardness, tensile strength and surface quality of Ti-6Al-4V," *Addit. Manuf.*, vol. 25, no. August 2018, pp. 176–186, 2019, https://doi.org/10.1016/j.addma.2018.09.002.
[48] A. Hadadzadeh, B. S. Amirkhiz, and M. Mohammadi, "Contribution of Mg2Si precipitates to the strength of direct metal laser sintered AlSi10Mg," *Mater. Sci. Eng. A*, vol. 739, no. August 2018, pp. 295–300, 2019, https://doi.org/10.1016/j.msea.2018.10.055.
[49] N. Hansen, "Hall-petch relation and boundary strengthening," *Scr. Mater.*, vol. 51, no. 8, pp. 801–806, 2004, https://doi.org/10.1016/j.scriptamat.2004.06.002.
[50] E. D. Cyr, A. Brahme, M. Mohammadi, R. K. Mishra, and K. Inal, "A new crystal plasticity framework to simulate the large strain behaviour of aluminum alloys at warm temperatures," *Mater. Sci. Eng. A*, vol. 727, no. June 2017, pp. 11–28, 2018, https://doi.org/10.1016/j.msea.2018.04.020.
[51] H. Mughrabi, "The α-factor in the Taylor flow-stress law in monotonic, cyclic and quasi-stationary deformations: dependence on slip mode, dislocation arrangement and density," *Curr. Opin. Solid State Mater. Sci.*, vol. 20, no. 6, pp. 411–420, 2016, https://doi.org/10.1016/j.cossms.2016.07.001.

The authors of this contribution

İstemihan Gökdağ
İstemihan Gökdağ received his BSc and MSc degrees in Mechanical Engineering from TOBB University of Economics and Technology in 2017 and 2021, respectively. He works at Turkish Aerospace Industries Inc., and his main fields of interests include additive manufacturing of aircraft structural components and topology optimization.

Erdem Acar
Dr. Erdem Acar is a professor in the Department of Mechanical Engineering, TOBB University of Economics and Technology, Ankara, Türkiye. His research interests include optimization, design of automobile and aircraft structures, finite element analysis, ballistic simulations, and uncertainty analysis. He is an associate fellow of the American Institute of Aeronautics and Astronautics (AIAA) and he has been serving as a Review Editor for the Journal of Structural and Multidisciplinary Optimization, Springer, since 2017.